TiO$_2$/g-C$_3$N$_4$ Binary Composite as an Efficient Photocatalyst for Biodiesel Production from Jatropha Oil and Dye Degradation

Abdul Basit Naveed, Aftab Javaid, Adeel Zia, Muhammad Tayyab Ishaq, Muhammad Amin,
Zia Ur Rahman Farooqi, and Azhar Mahmood*

Read Online

ACCESS | 📊 Metrics & More | 📰 Article Recommendations | 🔵 Supporting Information
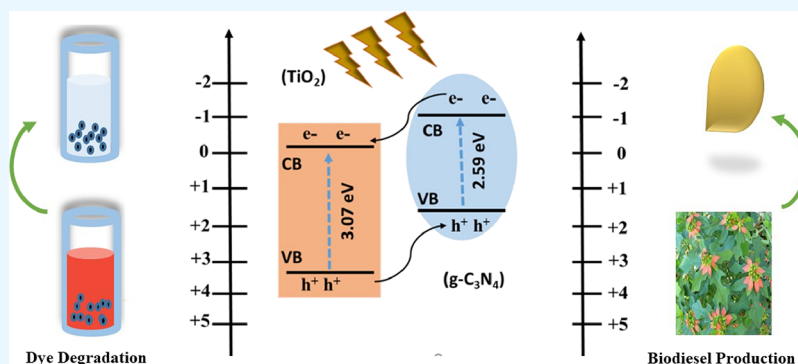
ABSTRACT: In the present work, TiO$_2$/g-C$_3$N$_4$ nanocomposites were synthesized by using highly crystalline TiO$_2$ nanorods/rice (NRs) and various percentages of g-C$_3$N$_4$ via a facile, scalable, and inexpensive pyrolysis method. The synthesized nanocomposites were characterized by various techniques, e.g., X-ray diffraction (XRD), scanning electron microscopy (SEM), energy-dispersive X-ray spectroscopy (EDX), N$_2$ adsorption and desorption analysis (BET), Fourier transform infrared spectroscopy (FTIR), UV−vis diffuse reflectance spectroscopy (DRS), electrochemical impedance spectroscopy (EIS), and chronoamperometry (CA). It was found that biodiesel production by the esterification reaction can be remarkably enhanced by coupling TiO$_2$ with g-C$_3$N$_4$; hereby, it was observed that with increasing percentage of g-C$_3$N$_4$ from 5 to 10 and 15% with respect to TiO$_2$ NRs, the photocatalytic activity rose and the maximum photocatalytic activity with 97% conversion was observed for NC-3, i.e., 15% g-C$_3$N$_4$/TiO$_2$. Moreover, the photoactivity of pristine TiO$_2$ NR aggregates was contrasted with their nanoparticle morphology and was estimated to be slightly better. When applied for photocatalytic Congo red dye degradation, this sample showed a 91% degradation efficiency using only a very small amount of the catalyst. The high catalytic efficiency is attributed to the narrow band gap, exceptionally high surface area, and efficient charge separation properties of the prepared catalysts.

1. INTRODUCTION

Environmental contamination and energy crisis are two of the major problems of the current society. An unchecked release of organic pollutants is contaminating freshwater resources.[1,2] Moreover, the high consumption of fossil fuels is also increasing environmental pollution; in particular, the elevated accumulation of greenhouse gases in our environment is a threat to life. To cope with this challenge, currently, the production of clean energy is being focused on. In addition, the shortage of petroleum resources and their high cost have forced us to look for alternate renewable energy resources. Biodiesel can be considered a renewable and sustainable energy source with low emissions of toxic pollutants.[3] It can be produced from different vegetable oils like cottonseed, sunflower, canola, palm, and soybean oils.[4] However, edible oils cannot be used as an energy source due to the high demand for them as food.[5] To overcome these issues, many non-edible oils can be considered renewable and sustainable

sources of biofuel production.[6−8] Among them, jatropha has unique characteristics of growing in every kind of land ranging from arid to semi-arid and sandy areas.[9]

The transesterification reaction is carried out for biodiesel production, in which jatropha oil and methanol are involved to produce fatty acid methyl esters (FAMEs).[10−12] The yield of biodiesel depends upon different reaction conditions such as the temperature of the reaction, amount and type of the catalyst, and methanol concentration.[13] Some homogeneous alkali catalysts can be applied for transesterification reactions,

e.g., NaOH and KOH under mild reaction conditions.[14] However, the base-catalyzed response is not suitable for biodiesel production because it leads to soap formation and hence lowers the biodiesel yield.[15] The acid-catalyzed reaction can be carried out to avoid saponification, but it is costly due to the excessive quantity of methanol and sophisticated equipment.[16,17] Recently, nanoparticles with smaller sizes and high surface areas have gained attention as catalysts in the transesterification reaction.[18,19] Semiconductor photocatalysts are used in transesterification reactions because photocatalysis is a productive process that proceeds under ambient conditions; e.g., it works under solar light and at room temperature.[14–17,20]

The consumption of organic dyes in the textile, leather, and plastic industries is rapidly increasing. These dyes have become a permanent part of wastewater and are difficult to remove by conventional wastewater treatment techniques. If untreated sewage is released into waterbodies, it causes many adverse effects on aquatic life. To mitigate these effects, photocatalysis is the most promising approach to degrading hazardous particles from wastewater to make them less harmful.[21–24]

In photocatalysis, TiO_2 is considered to be a more promising photocatalyst due to its stability, abundance, corrosion resistivity, and non-toxicity.[25] g-C_3N_4 is a non-toxic and metal-free photocatalyst, gaining much attention because of its appropriate band gap.[26–28] However, electron–hole recombination during photocatalysis is a drawback of most photocatalysts; another problem is the inefficient charge transport capability that decreases the photo-harnessing ability of photoactive materials like TiO_2 and g-C_3N_4.[29–31] This problem has been reported to reduce by variation in morphology, e.g., one-dimensional architectures of TiO_2, like nanorods, nanotubes, and nanobelts. One-dimensional nanostructures of TiO_2, especially TiO_2 nanorods, have distinctive properties like one-directional electron flow, high surface area, quantum confinement, and a more significant number of active sites.[32] Unfortunately, there are some limitations of TiO_2 regarding its photocatalytic performance as it works only under UV light (solar light contains only 4% UV light).[33] Many efforts have been made to make it visible light responsive to enhance its photocatalytic activity, for example, by heterojunction designing, surface modifications, and doping of metal and non-metal ions.[34,35] Heterojunction designing has been proven to be the best and most convenient strategy to increase photo-absorption of UV and visible wavelengths, which in turn increases photocatalytic efficacy by increasing the photocurrent intensity, reducing electron–hole recombination, and enhancing the surface potential of the involved materials.

Here, we synthesized g-C_3N_4/TiO_2 composites via a scalable one-step pyrolysis process and evaluated their photocatalytic activity for biodiesel production from jatropha oil and Congo red dye degradation. Furthermore, many factors impacting the yield of biodiesel production and dye degradation, e.g., alcohol to fatty acid molar ratio, temperature, reaction time, and weight percentage of the nanocomposite catalyst, were considered to attain the optimum conditions for enhanced photocatalytic activity of the catalysts.

2. MATERIALS AND METHODS

2.1. Chemicals. Titanium dioxide (TiO_2) powder/nanoparticles and sodium hydroxide (NaOH) were obtained from Merck. Hydrochloric acid (HCl, 37%) and melamine

($C_3H_6N_6$) were purchased from Sigma-Aldrich. All solvents, i.e., methanol, water, and acetone, were used after double distillation.

2.2. Synthesis of TiO_2 Nanorods. The hydrothermal method was used for the synthesis of TiO_2 nanorods. 3 g of TiO_2 was mixed with 100 mL of a NaOH solution (10 M) and stirred for 30 min. Then, the obtained mixture was poured into an autoclave and kept in an electric oven at 130 °C for 24 h. After that, the obtained precipitates were separated by centrifugation and washed with 0.1 M HCl and deionized water several times to attain a final pH of 7. The washed sample was placed into a vacuum oven to dry at 80 °C for 6 h. Calcination was done at 550 °C for 2 h to obtain TiO_2 nanorods/rice (NRs).

2.3. Synthesis of g-C_3N_4. g-C_3N_4 was prepared by the calcination of melamine in a heating furnace. 5 g of melamine was placed into a ceramic crucible and then kept at 550 °C for 2 h at a heating ramp of 5 °C/min. Finally, a light-yellow agglomerate was obtained, which was appropriately ground to get powdered g-C_3N_4.

2.4. Synthesis of g-C_3N_4/TiO_2 Nanocomposites. Dried samples of TiO_2 nanorods were mixed with melamine at different ratios and annealed at 550 °C (3 °C/min ramp rate) for 2 h in a muffle furnace. Three nanocomposites were prepared with 5, 10, and 15% g-C_3N_4 and were named NC-1 (5% g-C_3N_4/TiO_2), NC-2 (10% g-C_3N_4/TiO_2), and NC-3 (15% g-C_3N_4/TiO_2), respectively.

2.5. Characterizations. A Phillips PW3710 X-ray powder diffractometer with Cu Kα radiation (1.5406 Å) was used to probe the crystallinity of the nanocomposite. The morphological and elemental analysis was performed by scanning electron microscopy (SEM; Jeol JXA-840A) coupled with EDX. UV–vis diffuse reflection spectroscopy (DRS) (UV–vis PerkinElmer Lambda 9 spectrometer) and the Brunauer–Emmett–Teller (BET) method (NOVA 2200e) were applied to find the band gaps and the surface areas of the final products, respectively. Adsorbed impurities were removed by degassing the samples in a vacuum at 393 K for 4 h. The FTIR spectra of the synthesized catalysts were recorded by a Bruker Alpha FTIR spectrometer. Electrochemical impedance spectroscopy (EIS) and chronoamperometry in chopping mode were conducted with a Gamry Interface 3000 potentiostat with a three-electrode setup with a Ag/AgCl reference electrode, a platinum wire as the counter electrode, and nanomaterial drop-casted FTO film as the working electrode in a 0.5 M Na_2SO_3 aqueous electrolyte. A Thermo Scientific TSQ 8000 gas chromatography–mass spectrometry (GC–MS) chromatograph was employed to investigate the reaction products.

2.6. Evaluation of the Photocatalytic Activity. *2.6.1. Esterification of Jatropha Oil by Photocatalysis.* All of the synthesized photocatalysts were used for the esterification reaction. The reaction was performed at room temperature (25 °C) for 2 h in a simple photochemical reactor containing a 300 W xenon arc lamp as the light source. At room temperature, an ethanol and jatropha oil ratio of 10:1 was used with a dosage of 4% catalyst.

2.6.2. Dye Degradation. A series of experiments were performed to degrade the Congo red dye to check the photocatalytic activity of all of the synthesized catalysts. A 300 W xenon arc lamp was used as a light source and placed at a distance of 15 cm above the vessel, which contained a mixture of the Congo red dye and photocatalyst. To obtain visible light, a 400 nm cutoff filter was placed facing the reaction mixture.

Initially, a solution of 10 mg of the photocatalyst and 100 mg of Congo red was made in the dark. After continuous stirring for 10 min, the solution was placed under UV–vis light. After each 5 min time interval, 5 mL of the solution was taken out to check the percentage degradation efficiency of the catalyst.

3. RESULTS AND DISCUSSION

X-ray diffraction analysis was performed to investigate the crystal structure and effect of heating on the phase transition in TiO_2 (Figure 1). The signals at 2θ = 27.4, 36.1, 39.2, 41.2,
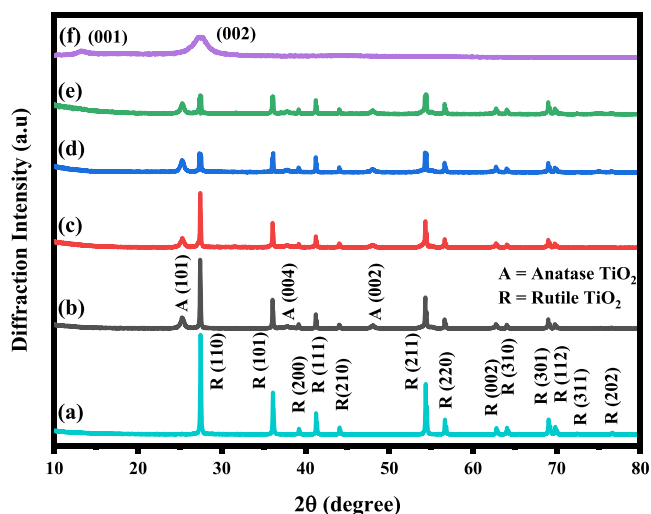
Figure 1. XRD results of (a) TiO_2 nanoparticles, (b) TiO_2 nanorods/rice, (c) NC-1, (d) NC-2, (e) NC-3, and (f) g-C_3N_4.

44.0, 54.3, 56.6, 62.8, 64.0, 69.0, 69.8, 72.4, and 76.5° correspond to the (110), (101), (200), (111), (210), (211), (220), (002), (310), (301), (112), (311), and (202) lattice planes of pure rutile phase TiO_2 (JCPDS 73-1764), respectively. TiO_2 NRs were synthesized via the hydrothermal method. The XRD spectrum reveals a few new peaks that appear at 2θ =25.2, 37.8, and 48.0° corresponding to the (101), (004), and (002) planes of the anatase phase. In addition, the peak intensities corresponding to the rutile phase of TiO_2 also get interrelatedly depressed, which demonstrates

the phase changing from rutile to anatase TiO_2. Thus, the TiO_2 NRs constitute a mixture of rutile and anatase phases. g-C_3N_4 exhibited two identification peaks at 2θ = 13.2 and 27.2° associated with the (001) and (002) planes accordingly. The g-C_3N_4/TiO_2 composites exhibit the same peak and validate the plausible statement that g-C_3N_4 has no impact on the crystallinity or phase purity.

The Spurr equation (eq 1) was used to probe the quantity of anatase in each of the samples.

$$F_r = \frac{1}{1 + 0.8\left[\frac{I_{A(101)}}{I_{R(110)}}\right]} \tag{1}$$

The intensities of the main rutile (110) and anatase (101) peaks were used to find the fraction of anatase in a sample. As specified above, the rutile-to-anatase phase transition happens after hydrothermal treatment; this change was investigated by using 100% rutile commercial TiO_2 NPs as precursor. A small increase in the anatase phase (30%) was observed after hydrothermal treatment, g-C_3N_4 mixing, and heating at a 550 °C temperature.

Figure 2,ba reveals the absorbance spectra and Kubelka–Munk-transformed reflectance spectra of commercial TiO_2 nanoparticles, TiO_2 NRs, NC-1, NC-2, NC-3, and g-C_3N_4. As the concentration of g-C_3N_4 is increased in samples, a remarkable redshift is observed as depicted in Figure 2a. Compared to the commercial TiO_2, the models containing g-C_3N_4 show apparent light absorption properties in the visible light region, with NC-1, NC-2, and NC-3 up to 418, 435, and 459 nm, respectively, which are due to the presence of g-C_3N_4. Figure 2b delineates the Kubelka–Munk-transformed reflectance spectra and optical absorption band gaps of the commercial TiO_2 nanoparticles, TiO_2 nanorods, NC-1, NC-2, NC-3, and g-C_3N_4. In TiO_2 nanorods, a slight increase in the band gap can be seen because of the mixed-phase (anatase and rutile) TiO_2 as compared to that of the commercial TiO_2 nanoparticles, which are pure rutile phase. The band gap of g-C_3N_4 is estimated to be 2.59 eV, and the band gaps of NC-1, NC-2, and NC-3 composites are evaluated to be 2.92, 2.81, and 2.75 eV, respectively, which are smaller than that of TiO_2 (Table 1). Hence, it is evident that the presence of g-C_3N_4 in the prepared nanocomposites contributes to narrowing down
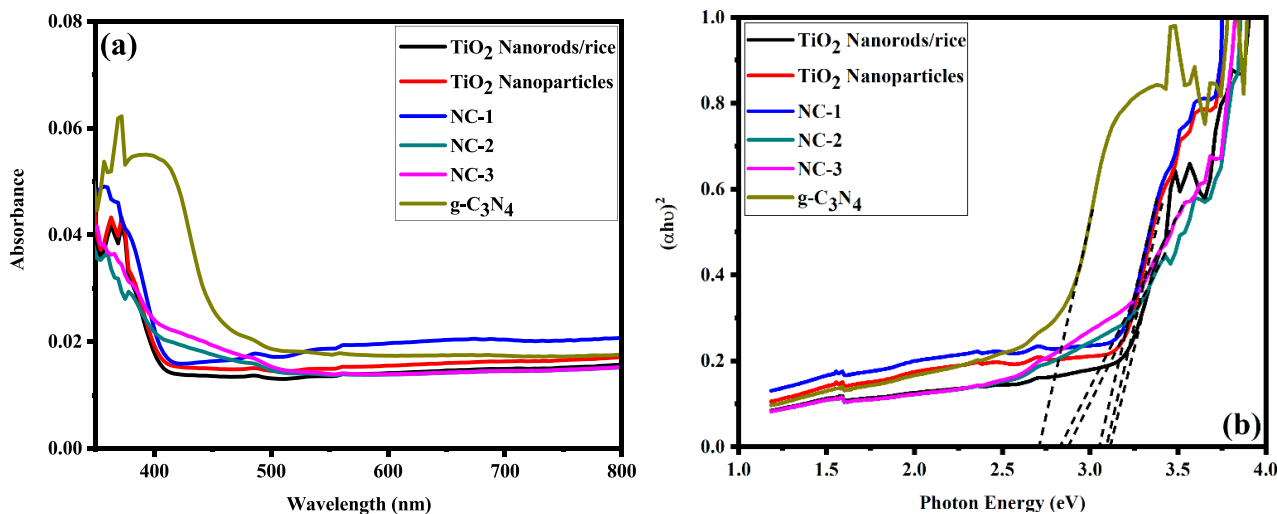
Figure 2. DRS results of (a) UV–visible absorbance and (b) Tauc's plot.

Table 1. Absorbance Maxima and Band Gaps

sample	wavelength (nm)	band gap (eV)
TiO_2 NPs	405	3.07
TiO_2 NRs	411	3.00
NC-1	418	2.92
NC-2	435	2.81
NC-3	459	2.75
g-C_3N_4	479	2.59

the band gap and consequently increasing the catalytic efficiency of the material.

Figure 3a shows spherical homogeneous particles of the commercial TiO_2 NPs. The morphology was controlled by the
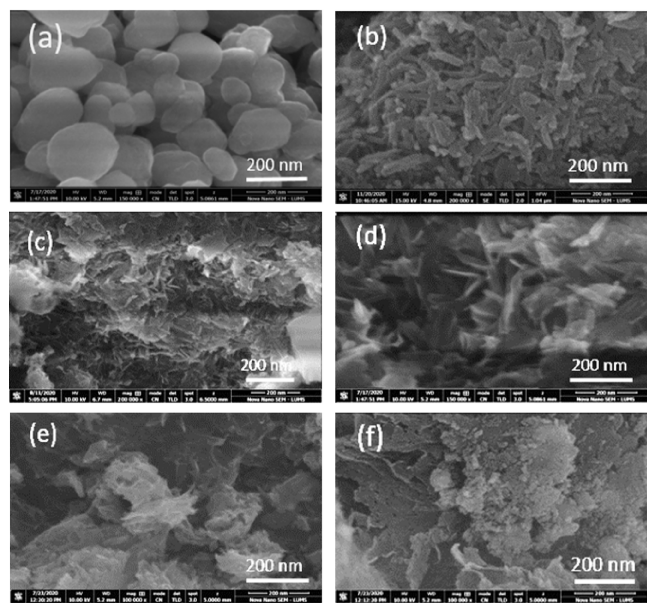
Figure 3. SEM images of (a) TiO_2 nanoparticles, (b) TiO_2 nanorods/rice, (c) NC-1, (d) NC-2, (e) NC-3, and (f) g-C_3N_4.

hydrothermal method to synthesize nanorods that appear to be nanorice. Figure 3b shows typical SEM images of TiO_2 nanorods. It was experimentally observed that g-C_3N_4 loading has a substantial impact on the morphology of the TiO_2 nanostructure. A high loading of g-C_3N_4 diminishes the rod features that are most likely due to the distinctive nucleation center provided by g-C_3N_4 (Figure 3c−e). At high concentrations of g-C_3N_4, the 2D nanoflakes have become the prominent morphology of the nanocomposite.

Elemental analysis was also performed to probe the elemental composition of the synthesized samples. The EDX spectrum revealed the characteristic peaks for Ti, O, C, and N; no peak was observed for any impurity (Figure 4). The atomic weight percentages of elements in each sample are summarized in Table 2.

Table 2. EDX Results and Atomic Weight Percentages of Different Elements

sample	Ti (wt %)	O (wt %)	C (wt %)	N (wt %)
TiO_2	60.1	39.9		
NC-1	36.1	54	3.9	6.8
NC-2	32	47.9	7.8	12.1
NC-3	42.3	26.6	11.7	18.2
g-C_3N_4			39.1	60.8

BET analysis was carried out to investigate the surface area and porosity of the photocatalysts. N_2 physisorption analysis was performed on commercial TiO_2 nanoparticles and morphology-controlled TiO_2 NRs.

Figure 5 displays the isotherms for each sample, which revealed remarkable enhancement in the surface area after converting the commercial TiO_2 nanoparticles to TiO_2 NRs through a hydrothermal process. The surface areas are 19.8 and 120.7 m^2 g^{-1} for TiO_2 nanoparticles and TiO_2 NRs, respectively, while the surface areas of NC-1, NC-2, and NC-3 are 106, 160.3, and 220.6 m^2 g^{-1}, respectively; as the photocatalytic efficiency is primarily based upon the surface area of the material, an enhanced surface area of the photocatalyst has therefore accelerated the rate of reaction
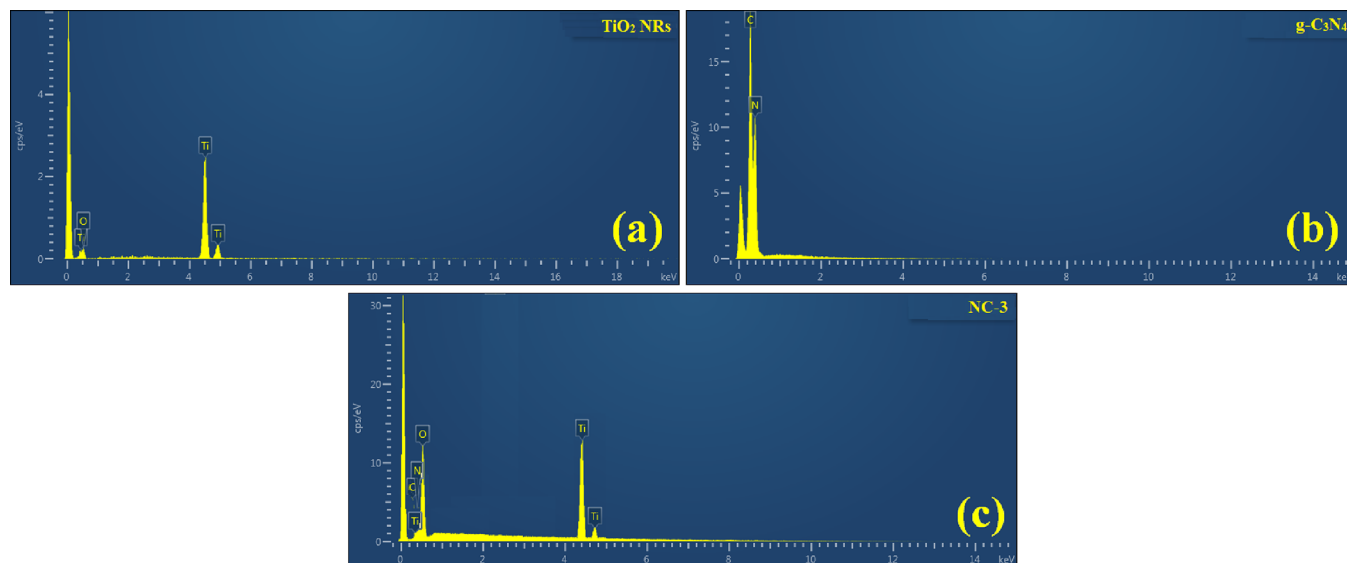
Figure 4. EDX of (a) TiO_2 NRs, (b) g-C_3N_4, and (c) NC-3 (most optimal).
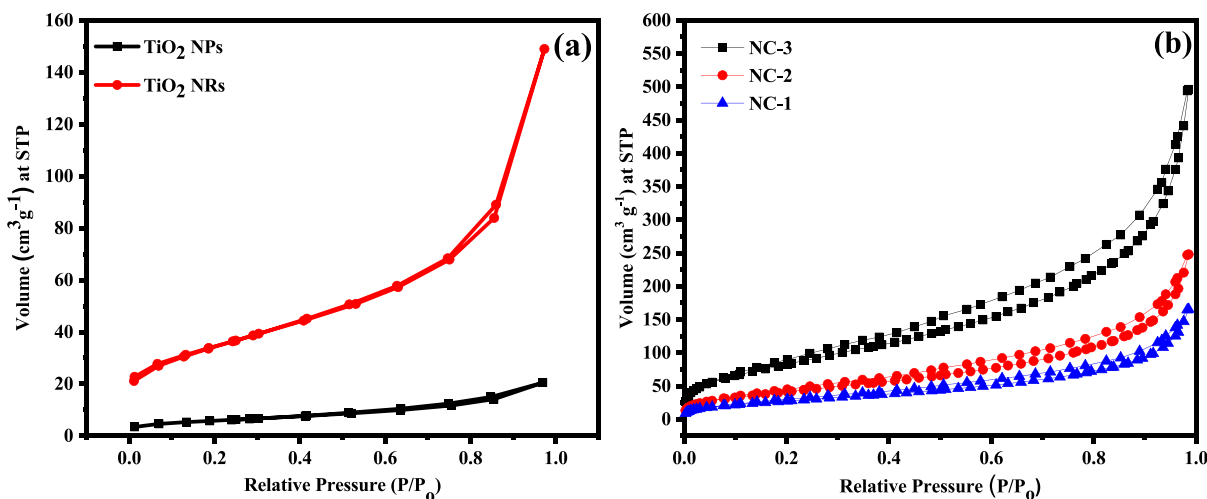
Figure 5. BET results: (a) nitrogen adsorption isotherms of TiO_2 NPs and TiO_2 NRs and (b) nitrogen adsorption isotherms of NC-1, NC-2, and NC-3.

by increasing the adsorption of O_2 (electron acceptor) and by utilizing electrons. The values of different physical parameters, e.g., surface area, pore volume, and pore width, are summarized in Table 3. It is also expected that some other factors such as

Table 3. Values of the Surface Areas of TiO_2 Nanoparticles, TiO_2 Nanorods, NC-1, NC-2, and NC-3

sample	surface area ($m^2 \ g^{-1}$)
TiO_2 nanoparticles	19.8
TiO_2 nanorods/rice	120.7
NC-1	106.0
NC-2	160.3
NC-3	220.6

particle size, ability to absorb light, and basicity of the catalyst also have an essential share in the enhancement of the catalytic activity.

FTIR spectra were used to validate the functional groups in TiO_2, g-C_3N_4, and g-C_3N_4/TiO_2 heterojunction photocatalysts. In the case of the pure TiO_2, the major peaks at $400-700$ cm^{-1} were observed due to Ti$-$O and Ti$-$O$-$Ti stretching modes, while in the case of g-C_3N_4, a broad peak at $3000-3300$ cm^{-1} confirmed the stretching modes of terminal NH_2 or NH groups. CN hetero-cycles exhibit characteristic absorption bands around $1200-1650$ cm^{-1}. Furthermore, the peak at 801 cm^{-1} was attributed to the breathing mode of the triazine units (Figure 6).

The charge-transfer resistance (R_{CT}) of as-prepared nanomaterials was determined to translate the effect of heterojunction formation in contrast to the bare materials under dark and illuminated situations. For photoactive materials, the charge-transfer resistance is interpreted through the size of the first semicircle obtained through EIS analysis; i.e., the larger the semicircle, the larger the charge-transfer resistance of the material under observation, and its charge-transfer capability remains inefficient. R_{CT} usually decreases upon the generation of a photocurrent when a photocatalyst is illuminated. In Figure 7, the R_{CT} values of the TiO_2 nanoparticles and NRs seem comparable and larger with respect to that of g-C_3N_4. Photocurrent generation decreases this R_{CT} value when light is shined on the electrode surface during the EIS. The R_{CT} values of illuminated TiO_2 NPs and NRs are suitably lower than those
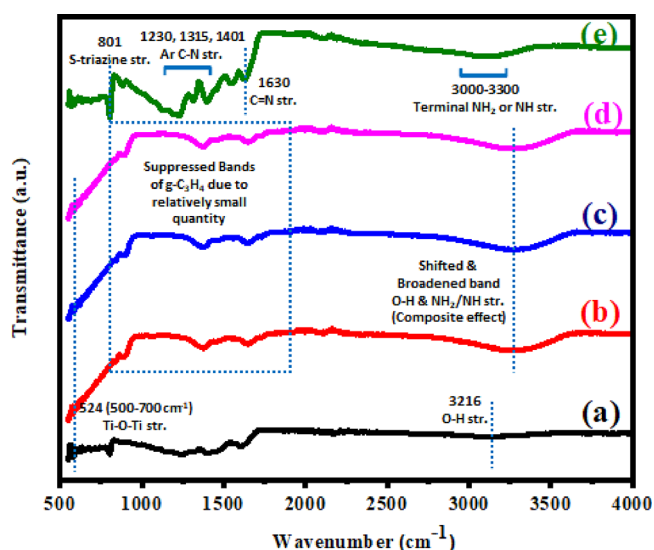
Figure 6. FTIR spectra of (a) TiO_2 nanorods/rice, (b) NC-1, (c) NC-2, (d) NC-3, and (e) g-C_3N_4.

of unilluminated ones, and the case of g-C_3N_4 is similar. Upon the formation of nanocomposites, the R_{CT} values of NC-1, NC-2, and NC-3 approach the R_{CT} value of g-C_3N_4, indicating better carrier transport through the composites as compared to those of their pristine constituents. After illumination of the electrodes holding the nanocomposites, the R_{CT} values of the respective samples are observed to be fairly decreased. This indicates that most of the photocurrent generated upon illumination gets transferred to the substrate molecules on the surface and charge recombination is decreased. The R_{CT} values of NC-1, NC-2, and NC-3 are observed to decrease, indicating that NC_3 represents the optimum ratio between g-C_3N_4 and TiO_2 NRs. This trend is also reinforced by the chronoamperometric data of the samples in chopping mode in Figure 8. The photocurrent order among the samples remains as $NC_3 > NC_2 > NC_1 > TiO_2$ NRs $\approx TiO_2$ NPs $> g$-C_3N_4. The photocurrent is observed to have values within tens to hundreds of microamperes. It can be observed from Figure 8 that the photocurrent generated on the metal oxide nanoparticles is relatively more stable than the one containing g-C_3N_4 as seen
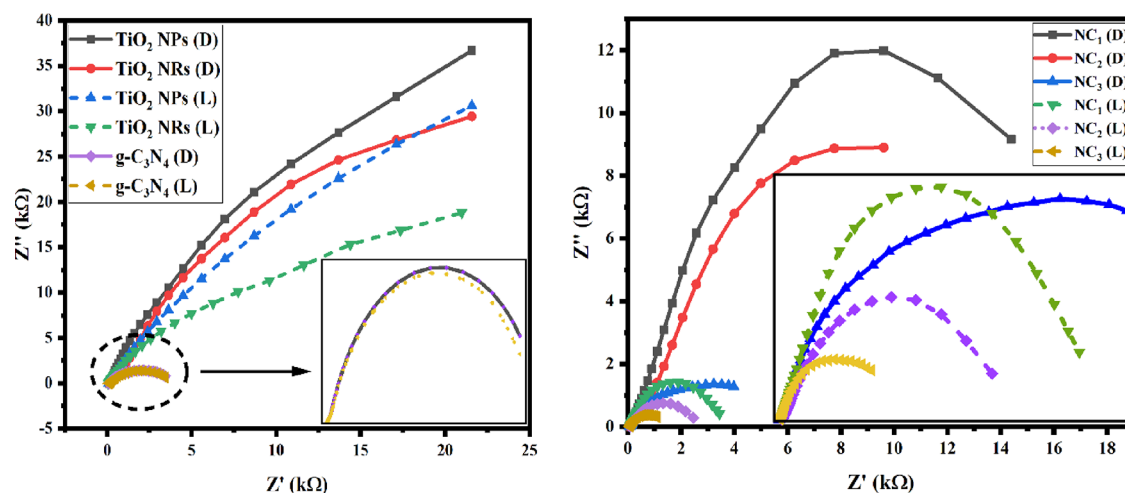
Figure 7. Electrochemical impedance spectra of pristine nanomaterials (left) and composites (right) in the dark (solid lines) and under illumination (dotted line).
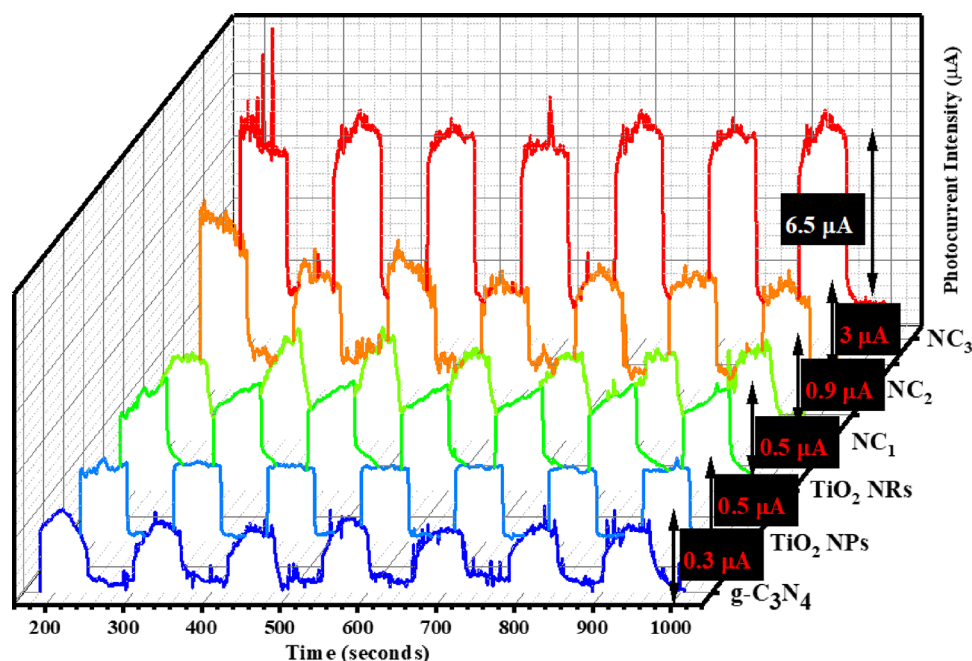
Figure 8. Chronoamperometric photocurrent information of the involved pristine photoactive materials and the nanocomposites.

through the fluctuations along the amperometry data, which indicates the intrinsic electronic stability associated with the metal oxide structures.

4. EVALUATION OF THE PHOTOCATALYTIC ACTIVITY

4.1. Analysis of the Conversion Efficiency by GC–MS.

GC–MS was used to investigate the conversion of jatropha oil into methyl ester and propose a mechanism for the esterification process.

4.1.1. Mechanism of Esterification. A photo-esterification reaction was carried out in the presence of the photocatalyst between methanol and jatropha oil. Methanol was chemically oxidized to $CH_3O^.$ at the valence band, while at the conduction band FFAs were reduced to $RCOOH^.$. The information related to band alignment has been taken from the literature and is presented in Figure 9.[36,37]
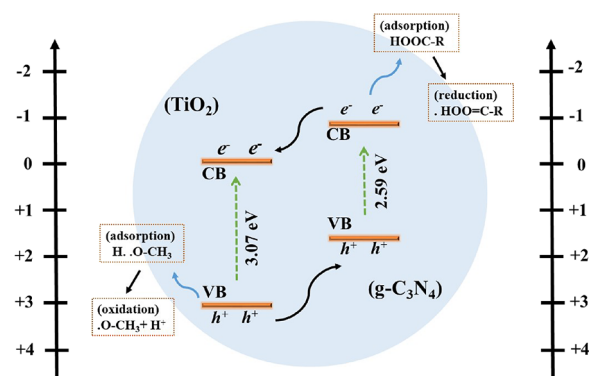
Figure 9. Band alignment between TiO_2 and g-C_3N_4.

All of the synthesized photocatalysts were used for esterification reactions (Figure 10). Pure jatropha oil contains
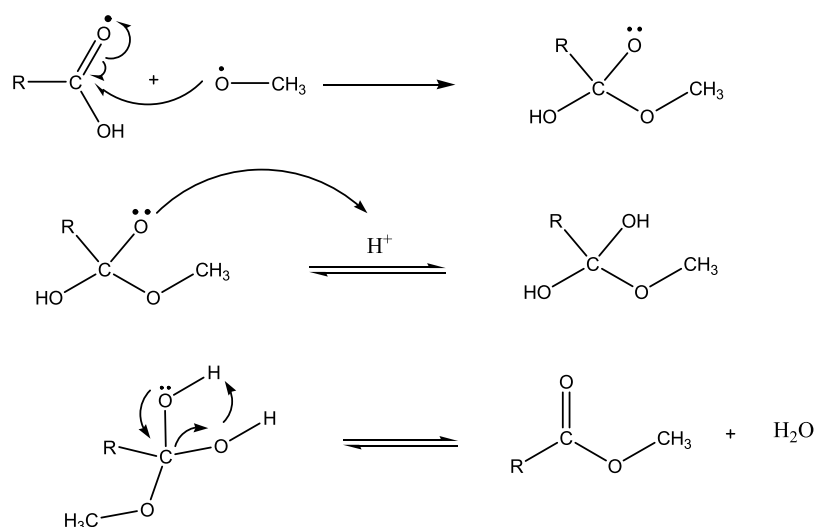
Figure 10. Scheme for the esterification of jatropha oil.

61% fatty acids (palmitic and stearic) and 29% methyl ester. In the photochemical reaction, the best photocatalytic activity was observed for the NC-3 sample, through which biodiesel with a 97% methyl ester concentration was obtained successfully as observed in Figure S1. The photocatalytic activity in terms of methyl ester percentage is given in Table 4 and also shown in Figure 11.

Table 4. Percentages of Methyl Ester before and after the Photochemical Reaction

samples	methyl ester before esterification (%)	methyl ester after esterification (%)
TiO_2 nanoparticles	29	63
TiO_2 nanorods/ rice	29	80
5% g-C_3N_4/ TiO_2	29	88
10% g-C_3N_4/ TiO_2	29	91
15% g-C_3N_4/TiO_2	29	97
g-C_3N_4	29	39
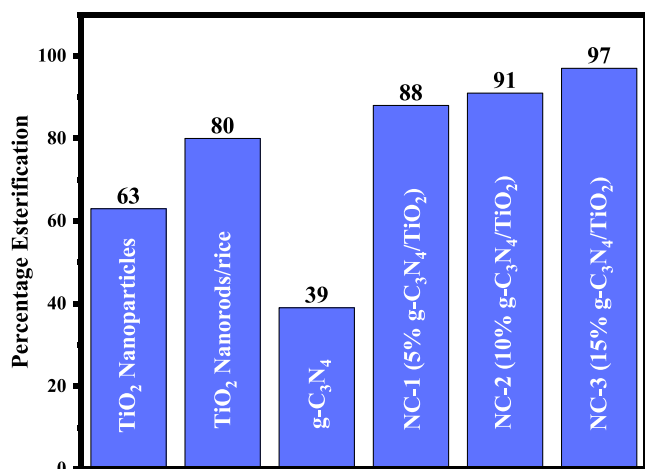
Figure 11. Percentages of methyl esters.

Various physical properties of the biodiesel, e.g., density, flash point, cloud point, boiling point, pour point, cetane number, kinematic viscosity, and sulfur content, were measured as shown in Table 5.

Table 5. Properties of Biodiesel Obtained from Jatropha Oil

density	0.905 g/cm^3
flash point	165 °C
cloud point	−6 °C
boiling point	333 °C
pour point	−15 °C
cetane number	57
kinematic viscosity	4.2 cSt
sulfur content	nil

4.2. Degradation of Congo Red Dye. We also checked the catalytic efficiency of our nanocomposites by the degradation of the Congo red dye. Figure 12 reveals the time-dependent percentage degradation of Congo red against time, by using g-C_3N_4, TiO_2, and their nanocomposites.
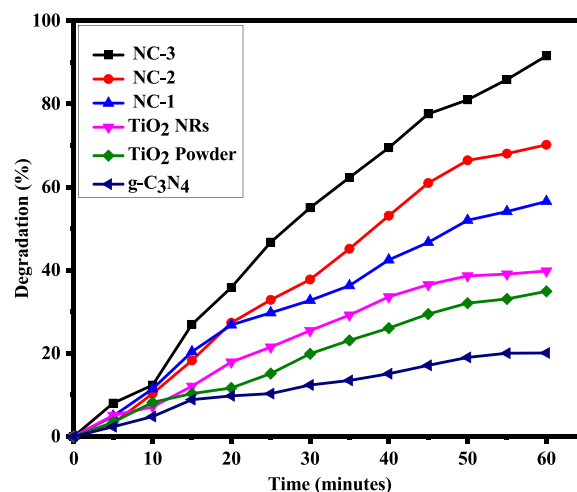
Figure 12. Percentage degradation plot of Congo red for the involved catalysts.
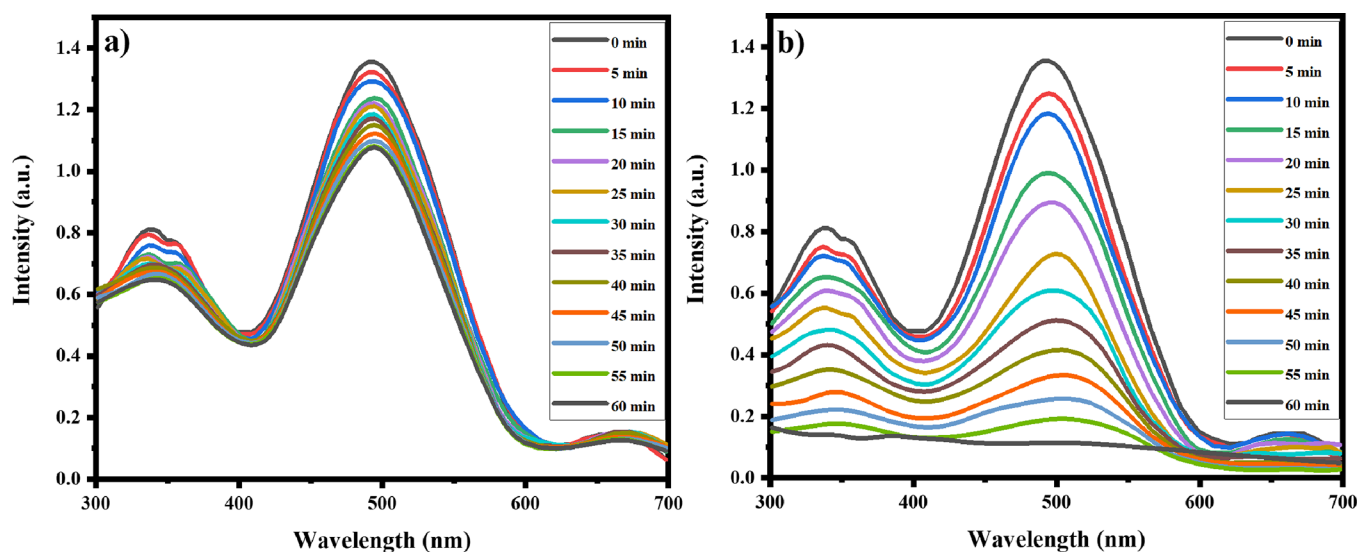
Figure 13. Congo red degradation spectra of (a) g-C$_3$N$_4$ and (b) NC-3 nanocomposites.

Equation 2 was used to calculate the % degradation of Congo red.

$$\eta\ (\%) = (A_o - A_t/A_o) \times 100 \qquad (2)$$

Here, A_o is the initial absorbance and A_t is the absorbance of the dye at time t.

g-C$_3$N$_4$ exhibits a band gap of 2.58 eV, so it can easily be excited by visible light. Upon excitation, electrons from the conduction band of g-C$_3$N$_4$ are transferred to the conduction band of TiO$_2$, leaving behind holes in the valence band of g-C$_3$N$_4$. Successful separation of charge carriers results in the improvement of the photocatalytic efficiency of the photocatalyst. Holes in the valence band combine with water and generate H$^+$ and OH$^.$. In contrast, the electrons present in the conduction band result in the generation of the O$_2^-$ (superoxide) radical, which further reacts with water and forms the OH$^.$ radical. These radicals carry out the degradation of the organic dyes. In bare TiO$_2$ NPs, TiO$_2$ NRs, and g-C$_3$N$_4$, the degradation efficiency is significantly lower than that of the composites of the photocatalyst, attributed to the rapid electron–hole recombination of these bare constituents, which ultimately results in their poor catalytic efficiency.

The 15% g-C$_3$N$_4$/TiO$_2$ composite demonstrated the best photocatalytic activity (Figure 12) among all of the samples due to the efficient charge separation, and the results can be explained based on the alignment of energy levels (see Figure 9). g-C$_3$N$_4$ absorbs visible light, and this results in the excitation of electrons to the conduction band, hence leaving holes in the valence band. In the synthesized composites, g-C$_3$N$_4$ can be irradiated by visible light and this property can be attributed to the suitable positions of the conduction band minimum (CBM) and valence band maximum (VBM). The electrons from the conduction band of g-C$_3$N$_4$ are transferred to the conduction band of TiO$_2$. This transfer of an electron from g-C$_3$N$_4$ to TiO$_2$ reduces the chances of electron–hole recombination and eventually considerably enhances the photocatalytic activity of the catalyst.

The photocatalytic degradation of Congo red was carried out for 60 min by using bare g-C$_3$N$_4$, bare TiO$_2$, and their nanocomposites (Figure 13a,b). A UV–visible spectrophotometer was used to calculate the λ_{max} value of the dye. It was observed that the degradation rates of pristine TiO$_2$ and g-

C$_3$N$_4$ nanomaterials were low under UV–visible irradiation, whereas an enhanced photocatalytic activity was observed when the g-C$_3$N$_4$/TiO$_2$ nanocomposite was used as a photocatalyst. When UV–visible light was applied to the mixture of the Congo red dye and g-C$_3$N$_4$/TiO$_2$ nanocomposite, we achieved 91% dye degradation within only 60 min of irradiation, which proves its very high degradation efficiency as compared to those of the pure TiO$_2$ and g-C$_3$N$_4$ samples.

It is clear from Figure 9 that the valance bands of g-C$_3$N$_4$ and TiO$_2$ are found at 1.7 and 3.1 V (SHE), respectively, while the conduction band position of g-C$_3$N$_4$ is way above 0 V (SHE). This indicates that the two materials can lead to the generation of reactive ions in an aqueous medium upon illumination. The CBM of g-C$_3$N$_4$ is capable of generating O$_2^{\bullet-}$ from dissolved oxygen, and the VBMs of both materials can generate OH$^\bullet$ species from water, which are thought to decolorize the dye via degradation pathways. Formation of heterojunctions between the two materials can form type II heterojunctions, leading to better separation of e–h pairs and enhanced degradation ability. These propositions appear to coincide with the observed percentage degradation. The proposed pathway is quoted from the literature (eqs 3–8).

$$g - C_3N_4 + TiO_2 \xrightarrow{h\upsilon} g - C_3N_4(h^+) + TiO_2(e^-) \qquad (3)$$

$$TiO_2(e^-) + O_2 \xrightarrow{h\upsilon} O_2^{\bullet-} + TiO_2 \qquad (4)$$

$$TiO_2(e^-) + O_2^{\bullet-} + 2H_2O \xrightarrow{h\upsilon} 2OH^- + 2OH^\bullet + TiO_2 \qquad (5)$$

$$g - C_3N_4(h^+) + OH^- + H_2O$$
$$\xrightarrow{h\upsilon} OH^\bullet + H^+ + g - C_3N_4 \qquad (6)$$

$$H^+ + O_2^{\bullet-} \xrightarrow{h\upsilon} HO_2^{\bullet-} \qquad (7)$$

$$Dye + O_2^{\bullet-} + OH^\bullet + HO_2^\bullet \xrightarrow{h\upsilon} Degraded\ Products \qquad (8)$$
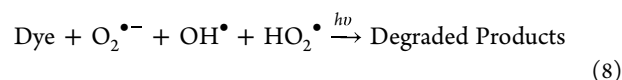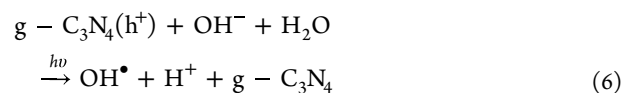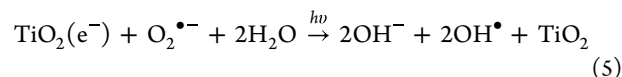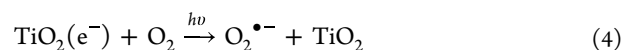
5. CONCLUSIONS

TiO$_2$ NRs were fabricated by a facile hydrothermal method, and g-C$_3$N$_4$ was synthesized via high-temperature calcination of melamine in a muffle furnace. A scalable in situ approach was used for the preparation of g-C$_3$N$_4$/TiO$_2$ nanocomposites in which melamine and TiO$_2$ NPs were mixed and calcined at 550 °C for 2 h. Various analytical techniques such as XRD, DRS, SEM, EDX, FTIR, BET, EIS, and CA were used to investigate the crystallinity, optical properties, morphology, elemental composition, surface area, charge-transfer resistance, and photoelectric capability of the synthesized material. The photocatalytic efficiencies of all of the synthesized catalysts were evaluated by the production of biodiesel as well as by the degradation of the Congo red dye. It is noted that the nanocomposites possess significantly higher photocatalytic activities as compared to their pristine counterparts due to their higher surface areas and efficient charge separation and carrier transport features. The present study reveals that the synthesis of nanocomposites for biodiesel production and organic dye degradation is an efficient method to cope with the challenges related to green energy and a clean environment.

ASSOCIATED CONTENT

Ⓢ Supporting Information

The Supporting Information is available free of charge at https://pubs.acs.org/doi/10.1021/acsomega.2c04841.

> Figure S1: Mass spectrograms of pure jatropha oil and the witnessed lowest esterification over g-C$_3$N$_4$ and the highest esterification efficiency achieved for the NC-3 composite (15% g-C$_3$N$_4$/TiO$_2$) (PDF)

AUTHOR INFORMATION

Corresponding Author

Azhar Mahmood − *Department of Chemistry, National University of Sciences and Technology (NUST), Islamabad 40100, Pakistan*; Email: dr.azhar@sns.nust.edu.pk

Authors

Abdul Basit Naveed − *Department of Chemistry, National University of Sciences and Technology (NUST), Islamabad 40100, Pakistan;* ⓘ orcid.org/0000-0001-8608-1275

Aftab Javaid − *Department of Chemistry, National University of Sciences and Technology (NUST), Islamabad 40100, Pakistan;* ⓘ orcid.org/0000-0002-0094-6723

Adeel Zia − *Department of Chemistry, National University of Sciences and Technology (NUST), Islamabad 40100, Pakistan*

Muhammad Tayyab Ishaq − *Department of Chemistry, National University of Sciences and Technology (NUST), Islamabad 40100, Pakistan;* ⓘ orcid.org/0000-0002-8907-0237

Muhammad Amin − *US-Pakistan Center for Advanced Studies in Energy, National University of Sciences and Technology (NUST), Islamabad 40100, Pakistan*

Zia Ur Rahman Farooqi − *Institute of Soil and Environmental Sciences, University of Agriculture, Faisalabad 38040, Pakistan*

Complete contact information is available at:
https://pubs.acs.org/10.1021/acsomega.2c04841

Notes

The authors declare no competing financial interest.

ACKNOWLEDGMENTS

REFERENCES

(1) Yang, Y.; Li, X.; Zhou, C.; Xiong, W.; Zeng, G.; Huang, D.; Zhang, C.; Wang, W.; Song, B.; Tang, X.; Li, X.; Guo, H. Recent Advances in Application of Graphitic Carbon Nitride-Based Catalysts for Degrading Organic Contaminants in Water through Advanced Oxidation Processes beyond Photocatalysis: A Critical Review. *Water Res.* **2020**, 116200.

(2) Zia, A.; Hamid, S.; Ehsan, M. F.; Allah, S. U.; Ashiq, M. N.; Shah, A. Congo Red Photomineralization over Co3O4/CoTe Common Cation Nanocomposites. *J. Mater. Sci.: Mater. Electron.* **2018**, *29*, 20271−20279.

(3) Saravanan, A.; Kumar, P. S.; Vo, D.-V. N.; Yaashikaa, P. R.; Karishma, S.; Jeevanantham, S.; Gayathri, B.; Bharathi, V. D. Photocatalysis for Removal of Environmental Pollutants and Fuel Production: A Review. *Environ. Chem. Lett.* **2021**, *19*, 441−463.

(4) Sharma, Y. C.; Singh, B.; Upadhyay, S. N. Advancements in Development and Characterization of Biodiesel: A Review. *Fuel* **2008**, *87*, 2355−2373.

(5) Corro, G.; Pal, U.; Tellez, N. Biodiesel Production from Jatropha Curcas Crude Oil Using ZnO/SiO2 Photocatalyst for Free Fatty Acids Esterification. *Appl. Catal., B* **2013**, *129*, 39−47.

(6) Kumar, A.; Sharma, S. An Evaluation of Multipurpose Oil Seed Crop for Industrial Uses (Jatropha Curcas L.): A Review. *Ind. Crops Prod.* **2008**, *28*, 1−10.

(7) Sharma, Y. C.; Singh, B. An Ideal Feedstock, Kusum (Schleichera Triguga) for Preparation of Biodiesel: Optimization of Parameters. *Fuel* **2010**, *89*, 1470−1474.

(8) Kegl, B. Experimental Investigation of Optimal Timing of the Diesel Engine Injection Pump Using Biodiesel Fuel. *Energy Fuels* **2006**, *20*, 1460−1470.

(9) Openshaw, K. A Review of Jatropha Curcas: An Oil Plant of Unfulfilled Promise. *Biomass Bioenergy* **2000**, *19*, 1−15.

(10) Russbueldt, B. M. E.; Hoelderich, W. F. New Rare Earth Oxide Catalysts for the Transesterification of Triglycerides with Methanol Resulting in Biodiesel and Pure Glycerol. *J. Catal.* **2010**, *271*, 290−304.

(11) Narasimharao, K.; Brown, D. R.; Lee, A. F.; Newman, A. D.; Siril, P. F.; Tavener, S. J.; Wilson, K. Structure−Activity Relations in Cs-Doped Heteropolyacid Catalysts for Biodiesel Production. *J. Catal.* **2007**, *248*, 226−234.

(12) López Granados, M.; Alba-Rubio, A. C.; Vila, F.; Martín Alonso, D. M.; Mariscal, R. Surface Chemical Promotion of Ca Oxide Catalysts in Biodiesel Production Reaction by the Addition of Monoglycerides Diglycerides and Glycerol. *J. Catal.* **2010**, *276*, 229−236.

(13) Guo, M.; Jiang, W.; Chen, C.; Qu, S.; Lu, J.; Yi, W.; Ding, J. Process Optimization of Biodiesel Production from Waste Cooking Oil by Esterification of Free Fatty Acids Using La3+/ZnO-TiO2 Photocatalyst. *Energy Convers. Manage.* **2021**, *229*, 113745.

(14) Smith, B.; Greenwell, H. C.; Whiting, A. Catalytic Upgrading of Tri-Glycerides and Fatty Acids to Transport Biofuels. *Energy Environ. Sci.* **2009**, *2*, 262−271.

(15) Du, L.; Ding, S.; Li, Z.; Lv, E.; Lu, J.; Ding, J. Trans-esterification of Castor Oil to Biodiesel Using NaY Zeolite-Supported La2O3 Catalysts. *Energy Convers. Manage.* **2018**, *173*, 728−734.

(16) Vyas, A. P.; Verma, J. L.; Subrahmanyam, N. A Review on FAME Production Processes. *Fuel* **2010**, *89*, 1−9.

(17) Zhang, Y.; Dubé, M. A.; McLean, D. D.; Kates, M. Biodiesel Production from Waste Cooking Oil: 1. Process Design and Technological Assessment. *Bioresour. Technol.* **2003**, *89*, 1−16.

(18) Pandya, H. N.; Parikh, S. P.; Shah, M. Comprehensive Review on Application of Various Nanoparticles for the Production of Biodiesel. *Energy Sources, Part A* **2022**, *44*, 1945−1958.

(19) Mofijur, M.; Siddiki, S. Y. A.; Shuvho, M. B. A.; Djavanroodi, F.; Fattah, I. M. R.; Ong, H. C.; Chowdhury, M. A.; Mahlia, T. M. I. Effect of Nanocatalysts on the Transesterification Reaction of First, Second and Third Generation Biodiesel Sources- A Mini-Review. *Chemosphere* **2021**, *270*, 128642.

(20) Corro, G.; Sánchez, N.; Pal, U.; Cebada, S.; Fierro, J. L. G. Solar-Irradiation Driven Biodiesel Production Using Cr/SiO2 Photocatalyst Exploiting Cooperative Interaction between Cr6+ and Cr3+ Moieties. *Appl. Catal., B* **2017**, *203*, 43−52.

(21) Naveed, A. B.; Riaz, F.; Mahmood, A.; Shahid, A.; Aqeel, S. A Facile Synthesis of Bi2O3/CoFe2O4 Nanocomposite with Improved Synergistic Photocatalytic Potential for Dye Degradation. *Catalysts* **2021**, *11*, 1180.

(22) Ehsan, M. F.; Bashir, S.; Hamid, S.; Zia, A.; Abbas, Y.; Umbreen, K.; Ashiq, M. N.; Shah, A. One-Pot Facile Synthesis of the ZnO/ZnSe Heterostructures for Efficient Photocatalytic Degradation of Azo Dye. *Appl. Surf. Sci.* **2018**, *459*, 194−200.

(23) Ehsan, M. F.; Qudoos, S.; Ahmad, Z.; Hamid, S.; Arfan, M.; Zia, A.; Umbreen, K.; Ashiq, M. N.; Tyagi, D. ZnTe/ZnSe Heterostructures: In-Situ Synthesis, Characterization and Photocatalytic Activity for Congo Red Degradation. *SN Appl. Sci.* **2019**, *1*, 197.

(24) Habibi-Yangjeh, A.; Asadzadeh-Khaneghah, S.; Feizpoor, S.; Rouhi, A. Review on Heterogeneous Photocatalytic Disinfection of Waterborne, Airborne, and Foodborne Viruses: Can We Win against Pathogenic Viruses? *J. Colloid Interface Sci.* **2020**, *580*, 503−514.

(25) Zhang, H.; Wang, X.; Li, N.; Xia, J.; Meng, Q.; Ding, J.; Lu, J. Synthesis and Characterization of TiO 2/Graphene Oxide Nanocomposites for Photoreduction of Heavy Metal Ions in Reverse Osmosis Concentrate. *RSC Adv.* **2018**, *8*, 34241−34251.

(26) Wen, J.; Xie, J.; Chen, X.; Li, X. A Review on G-C3N4-Based Photocatalysts. *Appl. Surf. Sci.* **2017**, *391*, 72−123.

(27) Akhundi, A.; Badiei, A.; Ziarani, G. M.; Habibi-Yangjeh, A.; Muñoz-Batista, M. J.; Luque, R. Graphitic Carbon Nitride-Based Photocatalysts: Toward Efficient Organic Transformation for Value-Added Chemicals Production. *Mol. Catal.* **2020**, *488*, 110902.

(28) Asadzadeh-Khaneghah, S.; Habibi-Yangjeh, A. G-C3N4/Carbon Dot-Based Nanocomposites Serve as Efficacious Photocatalysts for Environmental Purification and Energy Generation: A Review. *J. Cleaner Prod.* **2020**, *276*, 124319.

(29) Wang, J.; Wang, K.; He, Z.-H.; Li, S.-S.; Zhang, R.-R.; Guo, P.; Wang, W.; Yang, Y.; Liu, Z.-T. Solvent-Induced Synthesis of Hierarchical TiO2 Nanoflowers with Tunable Morphology by Monolayer Self-Assembly for Probing the Photocatalytic Performance. *J. Nanostruct. Chem.* **2021**, DOI: 10.1007/s40097-021-00445-2.

(30) Zhang, X.; Yang, P.; Jiang, S. P. Horizontally Growth of WS2/WO3 Heterostructures on Crystalline g-C3N4 Nanosheets towards Enhanced Photo/Electrochemical Performance. *J. Nanostruct. Chem.* **2021**, *11*, 367−380.

(31) Akhundi, A.; Habibi-Yangjeh, A.; Abitorabi, M.; Rahim Pouran, S. Review on Photocatalytic Conversion of Carbon Dioxide to Value-Added Compounds and Renewable Fuels by Graphitic Carbon Nitride-Based Photocatalysts. *Catal. Rev.* **2019**, *61*, 595−628.

(32) Fan, M.; Si, Z.; Sun, W.; Zhang, P. Sulfonated ZrO2-TiO2 Nanorods as Efficient Solid Acid Catalysts for Heterogeneous Esterification of Palmitic Acid. *Fuel* **2019**, *252*, 254−261.

(33) Tekin, D.; Birhan, D.; Kiziltas, H. Thermal, Photocatalytic, and Antibacterial Properties of Calcinated Nano-TiO2/Polymer Composites. *Mater. Chem. Phys.* **2020**, *251*, 123067.

(34) Mahy, J. G.; Lambert, S. D.; Tilkin, R. G.; Wolfs, C.; Poelman, D.; Devred, F.; Gaigneaux, E. M.; Douven, S. Ambient Temperature ZrO2-Doped TiO2 Crystalline Photocatalysts: Highly Efficient Powders and Films for Water Depollution. *Mater. Today Energy* **2019**, *13*, 312−322.

(35) Lin, G.-W.; Huang, Y.-H.; Tseng, W.; Lu, F.-H. Production of N-Doped Anatase TiO2 on TiN-Coated Ti Substrates by Plasma Electrolytic Oxidation for Visible-Light Photocatalysts. *Ceram. Int.* **2019**, *45*, 22506−22512.

(36) Acharya, R.; Parida, K. A Review on TiO2/g-C3N4 Visible-Light- Responsive Photocatalysts for Sustainable Energy Generation and Environmental Remediation. *J. Environ. Chem. Eng.* **2020**, *8*, 103896.

(37) Troppová, I.; Šihor, M.; Reli, M.; Ritz, M.; Praus, P.; Kočí, K. Unconventionally Prepared TiO2/g-C3N4 Photocatalysts for Photocatalytic Decomposition of Nitrous Oxide. *Appl. Surf. Sci.* **2018**, *430*, 335−347.